

Characterization of the Polarization Beam Response of SPT-3G Using Point Sources

T. DE HAAN,^{1,2} M. ARCHIPLEY,^{3,4} N. HUANG,⁵ A. J. ANDERSON,^{6,4,3} B. ANSARINEJAD,⁷ L. BALKENHOL,⁸ D. R. BARRON,⁹ K. BENABED,⁸ A. N. BENDER,^{10,4,3} B. A. BENSON,^{6,4,3} F. BIANCHINI,^{11,12,13} L. E. BLEEM,^{10,4,3} S. BOCQUET,¹⁴ F. R. BOUCHET,⁸ L. BRYANT,⁴ E. CAMPHUIS,⁸ M. G. CAMPITIELLO,¹⁰ J. E. CARLSTROM,^{4,15,16,10,3} J. CARRON,^{17,18} C. L. CHANG,^{10,4,3} P. CHAUBAL,⁷ P. M. CHICHURA,^{16,4} A. CHOKSHI,³ T.-L. CHOU,^{3,4,19} A. COERVER,⁵ T. M. CRAWFORD,^{3,4} C. DALEY,^{20,21} K. R. DIBERT,^{3,4} M. A. DOBBS,^{22,23} M. DOOHAN,⁷ A. DOUSSOT,⁸ D. DUTCHER,²⁴ W. EVERETT,²⁵ C. FENG,^{26,27} K. R. FERGUSON,^{28,29} N. C. FERREE,^{30,11,12} K. FICHMAN,^{16,4} A. FOSTER,²⁴ S. GALLI,⁸ A. E. GAMBREL,⁴ R. W. GARDNER,¹⁵ F. GE,^{30,11,12,31} N. GOECKNER-WALD,^{12,11} R. GUALTIERI,^{10,32} F. GUIDI,⁸ S. GUNS,⁵ N. W. HALVERSON,^{33,34} E. HIVON,⁸ A. Y. Q. HO,³⁵ G. P. HOLDER,³⁶ W. L. HOLZAPFEL,⁵ J. C. HOOD,⁴ A. HRYCIUK,^{16,4} F. KÉRUZORÉ,¹⁰ A. R. KHALIFE,⁸ L. KNOX,³¹ M. KORMAN,³⁷ K. KORNOELJE,^{3,4,10} C.-L. KUO,^{11,12,13} K. LEVY,⁷ Y. LI,⁴ A. E. LOWITZ,⁴ C. LU,³⁶ G. P. LYNCH,³¹ T. J. MACCARONE,³⁸ A. S. MANIYAR,^{11,12,13} E. S. MARTSEN,^{3,4} F. MENANTEAU,^{21,39} M. MILLEA,⁵ J. MONTGOMERY,²² Y. NAKATO,¹² T. NATOLI,⁴ G. I. NOBLE,^{40,41} Y. OMORI,^{3,4} A. OUELLETTE,³⁶ Z. PAN,^{10,4,16} P. PASCHOS,⁴ K. A. PHADKE,^{21,39,42} A. W. POLLAK,³ K. PRABHU,³¹ W. QUAN,^{10,16,4} M. RAHIMI,⁷ A. RAHILIN,^{3,4} C. L. REICHARDT,⁷ M. ROUBLE,²² J. E. RUHL,³⁷ E. SCHIAPPUCCI,⁷ A. C. SILVA OLIVEIRA,^{30,11,12} A. SIMPSON,^{3,4} J. A. SOBRIN,^{6,4} A. A. STARK,⁴³ J. STEPHEN,⁴ C. TANDOI,²¹ B. THORNE,³¹ C. TRENDAFILOVA,³⁹ C. UMITA,³⁶ J. D. VIEIRA,^{21,36,39} A. G. VIEREGG,^{4,3,15,16} A. VITRIER,⁸ Y. WAN,^{21,39} N. WHITEHORN,²⁹ W. L. K. WU,^{30,11,13} M. R. YOUNG,^{6,4} AND J. A. ZEBROWSKI^{4,3,6}

¹*Institute of Particle and Nuclear Studies (IPNS), High Energy Accelerator Research Organization (KEK), 1-1 Oho, Tsukuba, Ibaraki 305-0801, Japan*

²*International Center for Quantum-field Measurement Systems for Studies of the Universe and Particles (WPI-QUP), High Energy Accelerator Research Organization (KEK), 1-1 Oho, Tsukuba, Ibaraki 305-0801, Japan*

³*Department of Astronomy and Astrophysics, University of Chicago, 5640 South Ellis Avenue, Chicago, IL, 60637, USA*

⁴*Kavli Institute for Cosmological Physics, University of Chicago, 5640 South Ellis Avenue, Chicago, IL, 60637, USA*

⁵*Department of Physics, University of California, Berkeley, CA, 94720, USA*

⁶*Fermi National Accelerator Laboratory, MS209, P.O. Box 500, Batavia, IL, 60510, USA*

⁷*School of Physics, University of Melbourne, Parkville, VIC 3010, Australia*

⁸*Sorbonne Université, CNRS, UMR 7095, Institut d’Astrophysique de Paris, 98 bis bd Arago, 75014 Paris, France*

⁹*Department of Physics and Astronomy, University of New Mexico, Albuquerque, NM, 87131, USA*

¹⁰*High-Energy Physics Division, Argonne National Laboratory, 9700 South Cass Avenue, Lemont, IL, 60439, USA*

¹¹*Kavli Institute for Particle Astrophysics and Cosmology, Stanford University, 452 Lomita Mall, Stanford, CA, 94305, USA*

¹²*Department of Physics, Stanford University, 382 Via Pueblo Mall, Stanford, CA, 94305, USA*

¹³*SLAC National Accelerator Laboratory, 2575 Sand Hill Road, Menlo Park, CA, 94025, USA*

¹⁴*University Observatory, Faculty of Physics, Ludwig-Maximilians-Universität, Scheinerstr. 1, 81679 Munich, Germany*

¹⁵*Enrico Fermi Institute, University of Chicago, 5640 South Ellis Avenue, Chicago, IL, 60637, USA*

¹⁶*Department of Physics, University of Chicago, 5640 South Ellis Avenue, Chicago, IL, 60637, USA*

¹⁷*Université de Genève, Département de Physique Théorique, 24 Quai Ansermet, CH-1211 Genève 4, Switzerland*

¹⁸*Department of Physics & Astronomy, University of Sussex, Brighton BN1 9QH, UK*

¹⁹*National Taiwan University, No. 1, Sec. 4, Roosevelt Road, Taipei 106319, Taiwan*

²⁰*Université Paris-Saclay, Université Paris Cité, CEA, CNRS, AIM, 91191, Gif-sur-Yvette, France*

²¹*Department of Astronomy, University of Illinois Urbana-Champaign, 1002 West Green Street, Urbana, IL, 61801, USA*

²²*Department of Physics and McGill Space Institute, McGill University, 3600 Rue University, Montreal, Quebec H3A 2T8, Canada*

²³*Canadian Institute for Advanced Research, CIFAR Program in Gravity and the Extreme Universe, Toronto, ON, M5G 1Z8, Canada*

²⁴*Joseph Henry Laboratories of Physics, Jadwin Hall, Princeton University, Princeton, NJ 08544, USA*

²⁵*Department of Astrophysical and Planetary Sciences, University of Colorado, Boulder, CO, 80309, USA*

²⁶*Department of Astronomy, University of Science and Technology of China, Hefei 230026, China*

²⁷*School of Astronomy and Space Science, University of Science and Technology of China, Hefei 230026, China*

²⁸*Department of Physics and Astronomy, University of California, Los Angeles, CA, 90095, USA*

²⁹*Department of Physics and Astronomy, Michigan State University, East Lansing, MI 48824, USA*

³⁰*California Institute of Technology, 1200 East California Boulevard, Pasadena, CA, 91125, USA*

³¹*Department of Physics & Astronomy, University of California, One Shields Avenue, Davis, CA 95616, USA*

³²*Department of Physics and Astronomy, Northwestern University, 633 Clark St, Evanston, IL, 60208, USA*

³³*CASA, Department of Astrophysical and Planetary Sciences, University of Colorado, Boulder, CO, 80309, USA*

³⁴*Department of Physics, University of Colorado, Boulder, CO, 80309, USA*

³⁵*Department of Astronomy, Cornell University, Ithaca, NY 14853, USA*

³⁶*Department of Physics, University of Illinois Urbana-Champaign, 1110 West Green Street, Urbana, IL, 61801, USA*

³⁷*Department of Physics, Case Western Reserve University, Cleveland, OH, 44106, USA*

³⁸*Department of Physics & Astronomy, Box 41051, Texas Tech University, Lubbock TX 79409-1051, USA*

³⁹*Center for AstroPhysical Surveys, National Center for Supercomputing Applications, Urbana, IL, 61801, USA*

⁴⁰*Dunlap Institute for Astronomy & Astrophysics, University of Toronto, 50 St. George Street, Toronto, ON, M5S 3H4, Canada*

⁴¹*David A. Dunlap Department of Astronomy & Astrophysics, University of Toronto, 50 St. George Street, Toronto, ON, M5S 3H4, Canada*

⁴²*NSF-Simons AI Institute for the Sky (SkAI), 172 E. Chestnut St., Chicago, IL 60611, USA*

⁴³*Center for Astrophysics | Harvard & Smithsonian, 60 Garden Street, Cambridge, MA, 02138, USA*

Submitted to The Astrophysical Journal

ABSTRACT

Precise measurements of cosmic microwave background (CMB) polarization require rigorous control of instrumental systematics. For the South Pole Telescope’s third-generation camera (SPT-3G), which observes at 95, 150, and 220 GHz, accurate characterization of the beam—the instrument’s point spread function—is critical for understanding the polarized mm-wave sky. Here, we present direct measurements of SPT-3G’s polarized beam response using observations of 100 polarized extragalactic point sources. Previous SPT-3G CMB power spectrum analyses introduced a phenomenological parameter β_{pol} to describe the degree of polarization preserved in beam sidelobes. These analyses found evidence for significant depolarization driven by the requirement of polarization power spectrum consistency between different frequency bands. Our direct measurements yield $\beta_{\text{pol}} = 0.90 \pm 0.10$ at 95 GHz, 1.01 ± 0.12 at 150 GHz, and 0.81 ± 0.29 at 220 GHz, indicating minimal sidelobe depolarization. We validate these results through extensive systematic tests including Bayesian posterior sampling versus frequentist bootstrap resampling, real-space versus Fourier-space analysis, and variations on temperature-to-polarization leakage handling, covariance determination, and source selection. When compared to values inferred from previous cosmological analyses, which favored significant depolarization to resolve inter-frequency power spectrum inconsistencies, we find a mild tension of 1.9σ . However, this apparent discrepancy is dependent on the beam modeling, as our point source-based analysis derives much of its constraining power on β_{pol} from higher multipoles than the power spectrum analysis. These measurements therefore admit three explanations for the frequency-dependent residuals observed in the power spectrum analysis: a statistical fluctuation, the need for more sophisticated polarized beam models, or systematics other than beam depolarization.

Keywords: Cosmic microwave background — Cosmology: observations — Instrumentation: polarimeters

1. INTRODUCTION

Precise measurements of cosmic microwave background (CMB) polarization have emerged as powerful probes of fundamental physics, from constraining inflationary models through searches for primordial gravitational waves (P. A. R. Ade et al. 2021; M. Tristram et al. 2022; J. A. Zebrowski et al. 2025) to mapping the distribution of matter through gravitational lensing (Planck Collaboration et al. 2020, F. J. Qu et al. 2024). The South Pole Telescope’s third-generation camera (SPT-3G) represents a major advance in CMB polarimetry, deploying approximately 16,000 transition-edge sensor (TES) bolometers observing at 95, 150, and 220 GHz (B. A. Benson et al. 2014; J. A. Sobrin et al. 2022). Realizing the scientific potential of this instrument requires rigorous control of systematic uncertainties, including the characterization of the polarized beam response.

The instrumental beam—the angular response to a point source—directly affects measurements of CMB power spectra through its multiplicative nature. The beam profile consists of a central diffraction-limited main lobe and faint, extended sidelobes arising from mechanisms such as scattering from imperfect mirror surfaces, and diffraction from the gaps between primary mirror segments. While the main lobe is dominated by coherent optical processes that preserve polarization, the diverse physical origins of the sidelobes could theoretically lead to different polarization properties, such as depolarization from scattering. Traditionally, the polarization response has been modeled by factorizing the temperature beam with detector-specific polarization properties (efficiency and angle). However, F. Ge et al. (2025) demonstrated that this simple factorization fails to adequately explain observed SPT-3G CMB

power spectra. They introduced one phenomenological parameter β_{pol} per frequency band that interpolates between two limiting cases: $\beta_{\text{pol}} = 0$ corresponds to completely depolarized sidelobes (sidelobes respond only to temperature), while $\beta_{\text{pol}} = 1$ corresponds to identical sensitivity in temperature and polarization throughout the beam.

The cosmological analysis of [E. Camphuis et al. \(2025\)](#) (hereafter C25) found strong evidence for partial sidelobe depolarization, with a best-fit values under ΛCDM of $\beta_{\text{pol}}^{95} = 0.48 \pm 0.13$, $\beta_{\text{pol}}^{150} = 0.62 \pm 0.16$, and $\beta_{\text{pol}}^{220} = 0.62 \pm 0.15$. The frequency-combined detection of $\beta_{\text{pol}} < 1.0$ had a significance exceeding 5σ . This preference was driven primarily by the requirement of consistency between the 95, 150, and 220 GHz auto- and cross-spectra, largely independent of the assumed cosmological model (see Appendix B.2 of C25). Similar model-independent evidence was found in [F. Ge et al. \(2025\)](#), where constraints on β_{pol} were driven by the requirement of consistent fits to the EE power spectra across multiple frequency bands. However, these constraints were derived indirectly by marginalizing over β_{pol} within the power spectrum analysis itself; direct measurement of β_{pol} from independent data is required to test the hypothesis of sidelobe depolarization and to provide informative priors to sharpen future cosmological constraints.

Extragalactic radio sources provide useful probes of the polarized beam response. While limited by typically low polarization fractions ($\sim 2\%$), many are effectively point-like at SPT-3G’s angular resolution ($\sim 1'$) and sufficiently bright to constrain the polarization beam profile. By analyzing the radial profile of polarization signals around these sources, we can directly constrain how the polarization efficiency varies with angular distance from the beam center, measuring β_{pol} independently from CMB power spectrum analyses.

In this work, we present the first direct measurements of β_{pol} using 100 bright, polarized point sources observed by SPT-3G during the 2019–2023 observing seasons. Our analysis employs a simultaneous fitting framework that optimizes both beam parameters and source properties across multiple sources. We leverage modern computational tools including JAX for automatic differentiation and GPU acceleration to efficiently explore the high-dimensional parameter space. Extensive systematic tests validate the robustness of our measurements.

This paper is organized as follows. Section 2 describes the SPT-3G observations and data processing, including the treatment of bolometer time constants. Section 3 details our analysis methodology, covering beam parameterizations, the fitting procedure, and systematic tests.

Section 4 presents our measurements of β_{pol} and alternative beam characterizations. Section 5 discusses the physical interpretation and implications for cosmology, and we conclude in Section 6.

A companion paper (*Huang et al., in preparation*, hereafter H26) presents comprehensive SPT-3G beam measurements including the modeling used for the main beam determination used in this analysis.

2. OBSERVATIONS AND DATA

2.1. SPT-3G Instrument and Survey

The SPT-3G camera, installed on the 10-meter South Pole Telescope in austral summer 2016–2017, observes the sky with unprecedented sensitivity in three frequency bands centered at 95, 150, and 220 GHz ([B. A. Benson et al. 2014](#); [J. A. Sobrin et al. 2022](#)). The focal plane contains approximately 16,000 TES bolometers configured for polarization-sensitive observations, with each pixel containing six detectors sensitive to the three observing bands and two orthogonal linear polarization states. The beam full width at half maximum (FWHM) is approximately 1.6, 1.2, and 1.0 arcminutes at 95, 150, and 220 GHz, respectively.

This analysis uses data from the 2019–2023 observing seasons, comprising both the primary 1500 deg^2 survey field (“SPT-3G Main”) and three additional fields observed during austral summer totaling 2650 deg^2 (“SPT-3G Summer”). The corresponding temperature white-noise map depths are $(3.0, 2.5, 8.9) \mu\text{K-arcmin}$ at $(95, 150, 220) \text{ GHz}$ for the main field, and $(9.8, 9.2, 29.2) \mu\text{K-arcmin}$ for the summer fields ([K. Prabhu et al. 2024](#)).

2.2. Map Making and Data Processing

The time-ordered data (TOD) from individual detectors are processed into maps using the standard SPT-3G pipeline ([CMB-S4/SPT-3G Collaboration 2024](#)). The TOD are first filtered by fitting and subtracting polynomial and common-mode templates, as well as a basis of low-frequency Fourier modes. This filtering uses a 15 arcminute radius exclusion mask centered on the target point source, where data interior to the mask are excluded from template determination but the resulting templates are subtracted from all TOD. This masked filtering approach preserves the source emission at unity transfer function while partially removing contamination on scales larger than the $15'$ mask radius ($\ell \lesssim 720$), including primary CMB fluctuations and atmospheric noise.

Following filtering, the TOD are binned into Stokes T , Q , and U maps using inverse-variance weighting based on detector noise properties. We produce custom

$0.5^\circ \times 0.5^\circ$ maps at $0.1'$ pixel resolution approximately centered on each source position.

2.2.1. Treatment of Bolometer Time Constants

Since the cosmological analysis of C25, we have changed our approach to handling bolometer time constants (see e.g. [M. Archipley et al. 2025](#)). Bolometer time constants (typically ~ 5 ms) introduce a phase delay in detector response that effectively broadens the beam along the scan direction. In the C25 analysis, these effects were absorbed into an effective beam model. For this work, and as we transition to this approach for future SPT-3G power spectrum analyses, we deconvolve time constant effects at the TOD level using measured time constant values for each detector, cleanly separating optical beam properties from detector response characteristics.

2.2.2. Leakage Subtraction

Instrumental polarization—spurious polarization signals arising from temperature anisotropies—must be removed before analyzing the polarized beam. We construct empirical temperature-to-polarization leakage templates for each field through an iterative procedure. Initially, we normalize each source’s Q and U maps by its peak temperature flux density, then average these normalized maps across all sources with linear flux weighting to create ensemble-averaged leakage templates. These initial templates contain small contributions from true astrophysical polarization. To remove this contamination, we iterate: we fit the source and beam parameters using the framework described in Section 3.2, subtract the best-fit polarized signal model from each source’s Q and U maps, and then reconstruct the templates from these residual maps. This process converges sufficiently after a single iteration, though in practice we performed four.

Figure 1 shows the resulting leakage templates for the main survey field. In addition to linear temperature flux weighting, we implement three alternative weighting schemes for template construction (median, flat, and quadratic) and explore these as systematic tests in Section 3.4.

2.3. Point Source Selection

We identify the sample of point sources used for beam determination using a multi-step selection process. We begin with bright sources detected in SPT-3G temperature maps above a flux cutoff. For the main field, we choose a flux cutoff of > 200 mJy at 95 GHz. For the summer fields, we choose a lower flux cutoff to ensure a statistically robust sample size from each field. This initial selection yields 129 candidate sources. From this set,

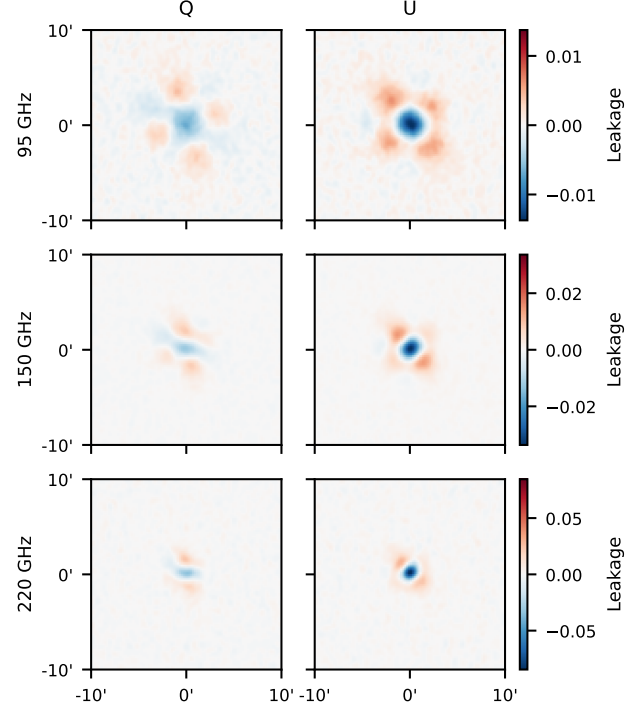


Figure 1. Empirical temperature-to-polarization leakage templates for the main field. These templates represent the spurious Q and U signal induced by a temperature point source, constructed by averaging source maps after subtracting the best-fit astrophysical polarization models. The structure of these templates is consistent with the leakage patterns identified in the cosmological analysis (see Figure 32 of [E. Camphuis et al. 2025](#)). These patterns are scaled by the source peak temperature and subtracted from each source prior to beam analysis.

we exclude 9 sources that appear extended or are associated with extended emission in visual inspection of the temperature map residuals (see the top-right panel of Figure 3 for an example that passes this check). We further exclude 11 sources which exhibit specific data quality issues, such as being located near the field boundaries where coverage is non-uniform. In such cases, the spatially varying noise levels would violate the stationarity assumptions required for our Fourier-domain analysis (Section 3.3.1). To facilitate a uniform multi-band analysis where the source position is determined with high signal-to-noise ($S/N \gg 10$) in every band, we exclude 3 sources with peak amplitudes $< 300 \mu\text{K}$ (approximately 15 mJy) in any of the three observing bands. Finally, we exclude 6 sources that have another bright source in the $0.5^\circ \times 0.5^\circ$ map, as that would contaminate the beam measurement.

The final sample contains 100 sources distributed across our survey fields: 46 from the main field and 54

from the summer fields. We retain sources regardless of their intrinsic polarization fraction; sources consistent with unpolarized emission provide constraints on temperature-to-polarization leakage (Section 2.2.2) and contribute to the empirical covariance estimation (Section 3.3.2). The sources span a range of properties, with some consistent with unpolarized emission and others up to 12% polarized. The majority of sources have polarization fractions in the 1%–3% range.

3. METHODOLOGY

3.1. Beam Models

Beam response functions can generally be described as two-dimensional or one-dimensional functions, expressible in either the harmonic or angular domain. In this work, we focus on the beam’s one-dimensional radial profile $B(r)$, where r represents the angular distance between the location of emission and the location of observation. We characterize this profile using two parameterizations: a regularized B-spline model (Section 3.1.1) with low model dependence and high parameter count, and the β_{pol} model (Section 3.1.2) with strong physical motivation and low parameter count.

This choice to focus on the radial profile is motivated by the downstream application: for the SPT-3G power-spectrum analysis, the leading-order effect of the beam on the isotropized bandpowers is entirely captured by this radial profile. The full two-dimensional beam will be presented in H26; here we isolate the purely radial degree of freedom that controls the overall multiplicative suppression of C_ℓ in T , E , and B .

3.1.1. B-spline Models

We establish a flexible, data-driven beam model using B-splines. B-splines provide a general basis for representing smooth functions while maintaining computational efficiency for optimization.

During the development of this analysis, our initial implementation used a pure B-spline basis: a peak-normalized linear combination of cubic B-spline functions spanning the radial range $r \in [0, 10']$ with linearly spaced knots. However, this model proved susceptible to overfitting in the beam core. Depending on the value of the modeled source position relative to the nearest pixel center, the $B(r = 0) = 1$ knot in the model affected the innermost 1–4 pixels (6–24 arcseconds), where the true signal varies smoothly at sub-pixel scales. The optimizer could exploit the parametric freedom to uniformly raise all source flux parameters and lower all $r \neq 0$ knots to create a small unphysical excursion in the beam core that fit noise fluctuations in these 1–4 pixels, improving χ^2 at the cost of introducing spurious structure.

To regularize the beam core while maintaining flexibility at larger radii, we adopt a hybrid parameterization containing a central normalized Gaussian, plus B-splines for $r > 0.25'$:

$$B(r) = \exp\left(-\frac{r^2}{2\sigma^2}\right) + \sum_{i=0}^N c_i \phi_i(r), \quad (1)$$

where the Gaussian component (with free parameter σ) describes the central beam ($r \leq 0.25'$) exclusively and the B-spline sum can modify this Gaussian at $r > 0.25'$. The B-spline basis functions $\{\phi_i(r)\}$ are constructed through a multi-step process to ensure proper regularization and numerical stability.

We begin with standard cubic B-splines ($k = 4$) defined on a clamped knot vector with interior knots spaced by $\Delta r = 0.4'$ between $r_{\min} = 0.25'$ and $r_{\max} = 10'$. To enforce smooth continuity with the Gaussian component, we impose the constraints $B(r_{\min}) = 0$ and $dB/dr(r_{\min}) = 0$. These constraints reduce the effective dimensionality of the B-spline parameter space.

We construct the constrained basis $\{\phi_i(r)\}$ by finding the null space of the constraint matrix via singular value decomposition. The resulting basis functions automatically satisfy the boundary conditions. To ensure numerical stability and interpretability, we orthonormalize these functions using 2D area normalization:

$$\int_0^\infty \phi_i(r) \phi_j(r) 2\pi r dr = \delta_{ij}, \quad (2)$$

The orthonormalization is performed via eigendecomposition of the Gram matrix computed using the area-weighted inner product.

The final model has $1 + 2N$ free parameters, where σ is shared between temperature and polarization beams, and $N = 22$ orthonormal B-spline coefficients (determined by the number of knots minus the number of constraints) are fit independently for the temperature beam and polarization beam.

The resulting temperature beam fit is combined with data from Saturn observations (details in H26) to construct $B_{\text{full}}(r)$ for the β_{pol} model described in Equation 3, while the polarization beam fit (Figure 4) provides an independent cross-check on that parameterization.

3.1.2. β_{pol} Model

Our primary beam model uses the β_{pol} parameterization introduced in F. Ge et al. (2025):

$$B_{\text{pol}}(r) = (1 - \beta_{\text{pol}})B_{\text{main}}(r) + \beta_{\text{pol}}B_{\text{full}}(r), \quad (3)$$

where $B_{\text{pol}}(r)$ is the polarization beam profile we wish to constrain. This interpolates between two limiting

cases: the main beam $B_{\text{main}}(r)$, which describes only the central diffraction-limited response, and the full beam $B_{\text{full}}(r)$, which includes both main beam and sidelobes as measured in temperature. The parameter β_{pol} quantifies the polarization efficiency of the sidelobes, with $\beta_{\text{pol}} = 0$ indicating completely depolarized sidelobes and $\beta_{\text{pol}} = 1$ indicating identical temperature and polarization response at all radii.

The full beam $B_{\text{full}}(r)$ combines the regularized B-spline temperature fit with data from dedicated Saturn observations that provide independent measurements at large radii ($r \gtrsim 3'$). This leverages the highly linear point source measurements in the beam core with the high signal-to-noise Saturn measurements of the sidelobes.

The main beam $B_{\text{main}}(r)$ is determined from a physical-optics model detailed in H26. This model accounts for the primary mirror, Lyot stop, and detector antenna patterns, parameterized by three free parameters that are fit simultaneously across all three observing bands using the innermost $0.75'$ of $B_{\text{full}}(r)$. The main beam model predicts the diffraction-limited response of an idealized optical system. While it naturally includes the near-sidelobe diffraction pattern, it contains no mechanism for producing anything close to the level of extended sidelobe power seen in the temperature data at $r \gtrsim 1'$.

The β_{pol} model thus has only one free parameter per frequency band, in contrast to the $1+2N$ parameters per band in the regularized B-spline model. This parsimony makes β_{pol} particularly valuable for cosmological analyses, where marginalizing over many beam parameters would significantly degrade cosmological constraints.

3.2. Fitting Framework

We determine beam parameters by simultaneously fitting the observed emission from all sources in our sample. For each source, we model the Stokes T , Q , and U maps as the convolution of a point source with the instrumental beam, treating both the source properties and beam parameters as free parameters in a joint optimization.

3.2.1. Model Parameterization

For a source at fitted position (x_0, y_0) with intrinsic Stokes parameters $(T_{\text{src}}, Q_{\text{src}}, U_{\text{src}})$, the model prediction at map position (x, y) is:

$$\begin{pmatrix} T_{\text{model}}(x, y) \\ Q_{\text{model}}(x, y) \\ U_{\text{model}}(x, y) \end{pmatrix} = \begin{pmatrix} B_{\text{full}}(r) T_{\text{src}} \\ B_{\text{pol}}(r) Q_{\text{src}} \\ B_{\text{pol}}(r) U_{\text{src}} \end{pmatrix}, \quad (4)$$

where $r = \sqrt{(x - x_0)^2 + (y - y_0)^2}$ is the angular distance from the fitted source position. The polarization beam $B_{\text{pol}}(r)$ differs depending on the beam model. This formulation assumes azimuthally symmetric beams and neglects instrumental polarization (which has been removed via the leakage subtraction procedure described in Section 2.2.2). We note that because the source Stokes amplitudes $(T_{\text{src}}, Q_{\text{src}}, U_{\text{src}})$ are free parameters optimized for each source, our measurement of the beam's radial profile shape is insensitive to global calibration factors in temperature or polarization efficiency. Any global miscalibration is absorbed into the fitted source amplitudes, leaving the normalized beam profile constraints unaffected.

3.2.2. Parameter Space

The full parameter vector $\boldsymbol{\theta}$ contains both the beam parameters and the source parameters. The beam parameters depend on whether the chosen model is the β_{pol} beam model or the regularized B-spline model, and whether the analysis is simultaneously fitting all bands or considering one band at a time.

For each point source, we fit five parameters per frequency band: the source positions (x_0, y_0) and the Stokes amplitudes $(T_{\text{src}}, Q_{\text{src}}, U_{\text{src}})$. For the full 100 sources, this yields 1500 source parameters that are optimized jointly with the beam parameters.

The total parameter count ranges from 501 (one-band, β_{pol}) to 1635 (three-band, regularized B-spline). This high-dimensional optimization is tractable due to the near-orthogonality of parameters, the presence of a single broad minimum, and the near-quadratic nature of that minimum. We leverage this structure through efficient gradient-based optimization as described in Section 3.3.4.

3.2.3. Coordinate Systems and Implementation

Source positions (x_0, y_0) are expressed in pixel coordinates relative to each source's map center, with bounds of ± 5 pixels ($\pm 0.5'$) from the nominal center. Source amplitudes are bounded to the range $(-5, 100)$ mK_{CMB} for both temperature and polarization. Both the position bounds and flux bounds were chosen to comfortably encompass the full range of observed source properties. Beam parameters are bounded to physically reasonable ranges. For β_{pol} , we allow the range $[-0.5, 2.0]$, B-spline coefficients are restricted to the range $[-0.5, 1.5]$, and the Gaussian width σ is bounded to $[0.1, 2.0]$ arcminutes. None of the results in this work depend on the precise choices of these bounds, as the χ^2 is extremely large everywhere on the hypercube boundary defined by these bounds.

Our bounds define a constrained optimization problem. To enable the use of efficient unconstrained gradient-based optimization algorithms (Section 3.3.4), we transform the bounded parameter space to an unconstrained space using a smooth bijective mapping. Specifically, we apply a scaled logit transformation:

$$\theta_{\text{unconstrained}} = \log \left(\frac{\theta - \theta_{\min}}{\theta_{\max} - \theta} \right). \quad (5)$$

This transformation maps the finite interval $[\theta_{\min}, \theta_{\max}]$ to the real line $(-\infty, \infty)$, ensuring that the optimizer steps always yield valid physical parameters.

3.3. Likelihood Formulation and Inference Methods

We evaluate beam and source parameters using maximum likelihood estimation, with uncertainties derived from bootstrap resampling. Our likelihood is based on a χ^2 statistic that compares observed maps to model predictions. We implement this χ^2 in both real space and Fourier space, and these implementations make different approximations about the noise properties and provide complementary systematic checks.

3.3.1. χ^2 Formulations

Both formulations assume Gaussian noise with a known covariance structure. The real-space formulation operates directly on map pixels:

$$\chi_{\text{real}}^2 = \sum_{x,y,\nu,s,\nu',s'} \Delta_{x,y}^{\nu,s} W_{x,y}^{\nu,s,\nu',s'} \Delta_{x,y}^{\nu',s'}, \quad (6)$$

where $\Delta_{x,y}^{\nu,s} = d_{x,y}^{\nu,s} - m_{x,y}^{\nu,s}$ is the residual between data and model at pixel (x,y) for frequency band ν and Stokes parameter $s \in \{T, Q, U\}$. The weight matrix $W_{x,y}^{\nu,s,\nu',s'}$ is the inverse covariance matrix (precision matrix) for that pixel, obtained from the map-making procedure. This matrix fully describes correlations between Stokes parameters within each band and pixel, but assumes independence between different pixels and between different bands. The pixel-independence assumption neglects the spatial correlations introduced by atmospheric noise and primary CMB fluctuations, but allows the weight matrix to vary spatially, capturing non-uniform noise properties across the map.

The Fourier-space formulation accounts for pixel-pixel correlations at the cost of assuming spatial stationarity:

$$\chi_{\text{Fourier}}^2 = \sum_{\vec{k},\nu,s,\nu',s'} \tilde{\Delta}_{\vec{k}}^{\nu,s*} (\mathbf{N}^{-1})_{\vec{k}}^{\nu,s,\nu',s'} \tilde{\Delta}_{\vec{k}}^{\nu',s'}, \quad (7)$$

where $\tilde{\Delta}_{\vec{k}}^{\nu,s} = \tilde{d}_{\vec{k}}^{\nu,s} - \tilde{m}_{\vec{k}}^{\nu,s}$ are the complex Fourier coefficients of the residuals at wavevector $\vec{k} = (k_x, k_y)$, and the asterisk denotes complex conjugation. The

precision matrix $(\mathbf{N}^{-1})_{\vec{k}}$ describes correlations between bands and Stokes parameters at each Fourier mode, naturally incorporating pixel-pixel correlations. However, this formulation assumes the noise properties are uniform across the map.

The complementary approximations in these two formulations provide a valuable consistency check: agreement between real-space and Fourier-space results validates that neither set of assumptions introduces significant bias. Our baseline analysis uses the Fourier-space formulation with the precision matrix determination described below, as it more accurately captures the dominant correlated noise sources (atmospheric fluctuations and CMB). The real-space formulation serves as a systematic cross-check; despite our expectation that noise properties are highly uniform within the cutouts, this analysis validates that the stationarity assumption in the baseline analysis does not introduce bias.

3.3.2. Fourier-Domain Precision Estimation

The Fourier-space precision matrix \mathbf{N}^{-1} is estimated from the input maps through an empirical procedure that accounts for both instrumental noise and the presence of primary CMB fluctuations.

First, we apply a noise mask to each input map. This mask consists of an apodization window at the map edges, combined with a circular excision around the source position. Both the map edges and the central circular cutout use a raised-cosine taper. The apodization suppresses edge effects in Fourier space, while the center excision removes the region dominated by the source signal, ensuring our noise estimate is not significantly contaminated by the signal we aim to measure.

We compute the discrete Fourier transform of each masked map and truncate the Fourier grid to modes with $k_x \leq k_{\max}$ and $k_y \leq k_{\max}$, with k_{\max} corresponding to $\ell = 31,000$, which maps to 85% of the Nyquist frequency of the TOD sampling, referred to sky coordinates at the highest-elevation, lowest-declination source. For each Fourier mode \vec{k} , we compute the empirical noise covariance matrix \mathbf{N}_{emp} by averaging over the N_{src} individual sources. The element corresponding to bands ν, ν' and Stokes parameters s, s' is calculated as:

$$(\mathbf{N}_{\text{emp}})_{\vec{k}}^{\nu,s,\nu',s'} = \frac{1}{N_{\text{src}}} \sum_{i=1}^{N_{\text{src}}} \tilde{d}_{\vec{k},i}^{\nu,s} \left(\tilde{d}_{\vec{k},i}^{\nu',s'} \right)^*, \quad (8)$$

where $\tilde{d}_{\vec{k},i}^{\nu,s}$ is the Fourier coefficient of the masked map for source i , band ν , and Stokes parameter s . This empirical covariance captures the average noise properties across the ensemble of observations. In order to account for differences in map depth, we group this procedure

by observing field, with each field receiving a separate ensemble average.

To establish a noise floor, we estimate the noise level from the region ($|\ell_y| > 4000$ and $4000 < |\ell_x| < 8000$) where the noise is lowest and demonstrates little k -dependence. We take the 20th percentile of the variance in this region for each band and Stokes parameter and refer to this as the white noise floor. We clip all variances to be no lower than the white noise floor, which affects $\ll 1\%$ of modes.

Our baseline covariance model combines theoretical CMB covariance with the empirical data covariance. The CMB covariance is computed from CAMB power spectra (A. Lewis et al. 2000) using a Planck 2018 cosmology (Planck Collaboration et al. 2020b). The angular power spectra C_ℓ^{TT} , C_ℓ^{EE} , C_ℓ^{BB} , and C_ℓ^{TE} are transformed to the (T, Q, U) basis via:

$$C_{\vec{k}}^{T,T} = C_\ell^{TT} \quad (9)$$

$$C_{\vec{k}}^{T,Q} = C_\ell^{TE} \cos(2\phi), \quad C_{\vec{k}}^{T,U} = C_\ell^{TE} \sin(2\phi) \quad (10)$$

$$C_{\vec{k}}^{Q,Q} = C_\ell^{EE} \cos^2(2\phi) + C_\ell^{BB} \sin^2(2\phi) \quad (11)$$

$$C_{\vec{k}}^{U,U} = C_\ell^{EE} \sin^2(2\phi) + C_\ell^{BB} \cos^2(2\phi) \quad (12)$$

$$C_{\vec{k}}^{Q,U} = (C_\ell^{EE} - C_\ell^{BB}) \sin(2\phi) \cos(2\phi) \quad (13)$$

where $\phi = \arctan(k_y/k_x)$, and $|\vec{k}|$ maps to ℓ in the flat-sky approximation and our choice of \vec{k} units. A raised-cosine high-pass filter is applied to the theoretical spectra to suppress fluctuations at $\ell \lesssim 720$, approximating the attenuation of modes larger than the mask size due to the TOD filtering. The angular power spectra are then interpolated onto a Fourier grid of the map, super-sampled by a factor of 4, then averaged down to the map resolution. The CMB covariance is then convolved with the apodization window function in the Fourier domain to account for mode coupling, and band-to-band covariances are constructed using band- and Stokes-dependent calibration factors from SPT-3G power spectrum analyses.

For diagonal elements of the covariance matrix, we take the element-wise maximum of the CMB-plus-white-noise model and the empirical covariance, ensuring we do not underestimate the noise. For off-diagonal elements, we use the CMB model. The elements of the correlation matrix are clipped to $[-0.95, 0.95]$ to ensure we do not rely on more than $20\times$ CMB suppression via band-band combinations. We find the resulting covariance matrix to be symmetric positive-definite for every mode. Finally, we invert each mode's covariance matrix to obtain the precision matrix $(\mathbf{N}^{-1})_{\vec{k}}$.

We also implement three alternative covariance models for cross-validation. The *data-driven diagonal model*

uses only the diagonal elements of the empirical covariance while neglecting band-band and Stokes-Stokes correlations. The *full data-driven model* uses the entire empirical covariance matrix including all correlations. The *white noise model* assumes uncorrelated noise across all non-zero modes, bands, and Stokes parameters, using only the measured white noise floor.

3.3.3. Bootstrap Uncertainty Estimation

Neither the real-space nor Fourier-space χ^2 formulation perfectly captures the statistical properties of our data. Therefore, a Bayesian exploration of the posterior assuming the noise model to be correct might underestimate uncertainties. We therefore employ bootstrap resampling to estimate parameter uncertainties. This bootstrap approach naturally accounts for potential contamination from marginally resolved sources, any mismatch between the assumed and true noise properties, source-to-source variations in noise properties, and effects such as the aforementioned pixel-pixel correlations in the real-space case or non-stationarity in the Fourier-space case.

We generate 200 bootstrap realizations by randomly resampling the 100 sources with replacement. For each realization, we re-optimize all parameters (both beam and source parameters) and record the resulting best-fit beam parameters. The sample covariance of these 200 bootstrap estimates provides our uncertainty estimate and parameter covariance matrix.

3.3.4. Optimization and Sampling

We explore the likelihood surface using both optimization (to find the maximum likelihood point) and Markov chain Monte Carlo sampling (to characterize the full posterior distribution).

For optimization, we employ adaptive moment estimation algorithms. We use a two-stage approach: an initial phase with Adam (Adaptive Moment Estimation, D. P. Kingma & J. Ba 2017) followed by a refinement phase with AMSGrad (S. J. Reddi et al. 2019), a variant that prevents the effective learning rate from increasing inappropriately when parameters become well-converged. This combination provides rapid and robust convergence across the high-dimensional parameter space.

For posterior sampling, we use microcanonical Langevin Monte Carlo (MCLMC, J. Robnik et al. 2023), an efficient Hamiltonian Monte Carlo variant. We also validated results using the No-U-Turn Sampler (NUTS, M. D. Hoffman & A. Gelman 2011), finding excellent agreement but superior efficiency with MCLMC.

All optimization and sampling is performed in a transformed parameter space designed for efficiency. Starting from the bounded physical parameters, we first apply

the logit transformation (Section 3.2) to map to an unbounded space. We then scale each parameter by the inverse square root of its curvature (second derivative of χ^2). This scaling makes the likelihood surface nearly isotropic, enabling efficient exploration.

For MCMC sampling, we explicitly include the Jacobian of both transformations in the likelihood to ensure samples are drawn from the correct posterior distribution with an effective flat prior on the physical parameters. The near-diagonal curvature matrix (with typical off-diagonal correlations < 0.1) validates our choice to scale by the diagonal curvature alone rather than computing the full Hessian, which would be too computationally expensive.

3.3.5. Algorithmic Summary

We summarize the baseline analysis pipeline in Algorithm 1. This procedure combines the iterative leakage removal, covariance estimation, and optimization procedures described in Sections 2–3.3.

3.4. Systematic Tests

We perform extensive systematic tests to validate our baseline analysis and assess robustness to methodological choices. Our baseline uses the Fourier-space χ^2 with CMB-informed precision matrices (Section 3.3.2), bootstrap uncertainties (Section 3.3.3), and linear flux weighting for leakage templates.

The systematic variations described below provide alternative analysis approaches that, while potentially having larger uncertainties, should yield unbiased estimates of the beam parameters.

3.4.1. Temperature Beam Validation

As a fundamental cross-check of our methodology, we apply the β_{pol} interpolation framework to the temperature data. We fit for β_T in the temperature beam:

$$B_T(r) = (1 - \beta_T)B_{\text{main}}(r) + \beta_T B_{\text{full}}(r), \quad (14)$$

analogous to Equation 3 for polarization. Since $B_{\text{full}}(r)$ is constructed from the same temperature observations (supplemented by Saturn data), this analysis is circular by design. We therefore expect $\beta_T \approx 1.0$ with residuals driven only by the addition of Saturn data and numerical limitations, rather than statistical scatter. This provides an internal consistency check: if our fitting framework incorrectly recovers beam parameters, it should manifest equally in temperature and polarization.

We find $\beta_T^{95} = 1.000 \pm 0.032$, $\beta_T^{150} = 0.996 \pm 0.021$, and $\beta_T^{220} = 0.994 \pm 0.024$, which are all consistent with unity at $\lesssim 0.2\sigma$. The high accuracy confirms that our methodology correctly recovers known beam properties.

Algorithm 1: Baseline Analysis

```

Require: Sources  $\mathcal{D} = \{\mathbf{d}_i\}_{i=1}^N$   

    over bands  $\nu \in \{95, 150, 220\}$ ; Stokes  $s \in \{T, Q, U\}$   

Require: Beam templates  $B_{\text{main}}(r)$ ,  $B_{\text{full}}(r)$ ; CMB  $C_\ell$ 

Subroutine: Joint Optimization (Sec. 3.3.4)
1: function JOINTFIT( $\mathcal{D}_{\text{in}}$ ,  $\mathbf{N}^{-1}$ )
2: Define  $\boldsymbol{\theta} = [\beta_{\text{pol}}^{95}, \beta_{\text{pol}}^{150}, \beta_{\text{pol}}^{220}, \phi_1^{95}, \dots, \phi_N^{220}]$ 
3: where  $\phi_i^\nu = (x, y, T, Q, U)_i^\nu$  for source  $i$ , band  $\nu$ 
4: Construct  $B_{\text{pol}}(r; \beta_{\text{pol}}^\nu)$  (Eq. 3)
5: Generate model maps  $m_i(\vec{x}; \phi_i^\nu, B_{\text{pol}}^\nu)$ 
6:  $\tilde{\Delta}_{\vec{k}, i} \leftarrow \text{FFT}(\mathbf{d}_i - m_i)$ 
7:  $\chi^2(\boldsymbol{\theta}) \leftarrow \sum_{i, \vec{k}} \tilde{\Delta}_{\vec{k}, i}^\dagger \mathbf{N}_{\vec{k}}^{-1} \tilde{\Delta}_{\vec{k}, i}$ 
8: Transform  $\boldsymbol{\theta}$  to unbounded space
9:  $\boldsymbol{\theta}^* \leftarrow \text{Adam}(\nabla \chi^2, \boldsymbol{\theta}_{\text{init}})$ 
10:  $\hat{\boldsymbol{\theta}} \leftarrow \text{AMSGrad}(\nabla \chi^2, \boldsymbol{\theta}^*)$ 
11: return  $\hat{\boldsymbol{\theta}}$ 

Maximum Likelihood Analysis (Sec. 2.2.2–3.2)
12: Init  $\mathbf{L}_s \leftarrow \text{WeightedMean}(\mathcal{D})_s$  for  $s \in \{Q, U\}$ 
13: for  $j \leftarrow 1$  to 5 do
14:  $\mathcal{D}_{\text{corr}} \leftarrow \{\mathbf{d}_i - \mathbf{L}\}_{i=1}^N$ 
15:  $\mathbf{C}_{\text{emp}} \leftarrow \text{Cov}(\text{Mask}(\mathcal{D}_{\text{corr}}))$ 
16:  $\mathbf{C}_{\text{CMB}} \leftarrow \text{SumWithModeCoupling}(C_\ell)$ 
17: for each mode  $\vec{k}$  do
18:  $\mathbf{D}_{\vec{k}} \leftarrow \text{Max}(\text{diag}(\mathbf{C}_{\text{emp}}(\vec{k})), \text{diag}(\mathbf{C}_{\text{CMB}}(\vec{k})))$ 
19:  $\mathbf{N}_{\vec{k}}^{-1} \leftarrow (\mathbf{D}_{\vec{k}} + \text{OffDiag}(\mathbf{C}_{\text{CMB}}(\vec{k})))^{-1}$ 
20:  $\hat{\boldsymbol{\theta}} \leftarrow \text{JOINTFIT}(\mathcal{D}_{\text{corr}}, \mathbf{N}^{-1})$ 
21:  $\mathbf{M}_i \leftarrow \text{Model}(\hat{\boldsymbol{\theta}}, i)$ 
22:  $\mathbf{L} \leftarrow \text{WeightedMean}(\{\mathbf{d}_i - \mathbf{M}_i\}_{i=1}^N)$ 
23:  $\hat{\boldsymbol{\theta}}_{\text{data}} \leftarrow \hat{\boldsymbol{\theta}}$ 

Uncertainty Estimation (Sec. 3.3.3)
24:  $\boldsymbol{\Theta}_{\text{boot}} \leftarrow \emptyset$ 
25: for  $b \leftarrow 1$  to  $N_{\text{boot}}$  do
26:  $\mathcal{D}^* \leftarrow \text{ResampleWithReplacement}(\mathcal{D}_{\text{corr}})$ 
27:  $\hat{\boldsymbol{\theta}}^* \leftarrow \text{JOINTFIT}(\mathcal{D}^*, \mathbf{N}^{-1})$ 
28:  $\boldsymbol{\Theta}_{\text{boot}} \leftarrow \boldsymbol{\Theta}_{\text{boot}} \cup \{\hat{\boldsymbol{\theta}}^*\}$ 

return  $\mu = \hat{\boldsymbol{\theta}}_{\text{data}}$ ,  $\Sigma = \text{Cov}(\boldsymbol{\Theta}_{\text{boot}})$ 

```

3.4.2. Simulation Validation

We validate the analysis pipeline through end-to-end simulations. We generate mock source maps with known input parameters: specified beam profiles (both β_{pol} and Gaussian+B-spline models), source positions with $\sim 0.1'$ offsets from map centers, and Stokes parameters spanning the range of observed source properties. The beam fitting analysis pipeline is then applied to these simulated sources. We find negligible systematic offsets, confirming that our implementation is free of significant coding errors or numerical artifacts and that the analysis framework is self-consistent.

3.4.3. Posterior Distribution Characterization

To validate our use of maximum-likelihood optimization with bootstrap uncertainties, we perform the MCLMC Bayesian analysis from Section 3.3.4. We generate 20,000 posterior samples after 5,000 adaptation steps to burn in and determine the trajectory length and step size. We use the resulting posterior samples to compute marginalized posterior distributions for all parameters.

Visual inspection of two-dimensional posterior slices for parameter pairs with the highest correlation coefficients shows that all posteriors are well-approximated by multivariate Gaussians with minimal off-diagonal correlations ($\rho \lesssim 0.3$). The marginalized beam parameter posteriors show good overlap with the bootstrap distributions, though they are not identical as the Bayesian posterior and frequentist bootstrap distributions answer fundamentally different statistical questions. The near-Gaussian posteriors validate our approximation that the likelihood surface is sufficiently well-behaved to justify maximum-likelihood estimation with bootstrap uncertainties.

3.4.4. Real-Space Analysis

Using the pixel-space χ^2 (Section 3.3.1) with pixel-level precision matrices from map-making, we find consistent results with the baseline analysis. This analysis neglects pixel-pixel correlations but allows for spatially varying noise.

3.4.5. Alternative Precision Matrices

Using the three alternative precision matrices described in Section 3.3.2 (data-driven diagonal, fully data-driven, and white noise) in the Fourier-space χ^2 , we also find β_{pol} constraints consistent with the baseline analysis. The white noise assumption in particular gives much larger uncertainties, though the results remain statistically consistent. This agreement validates our baseline precision matrix.

3.4.6. Leakage Template Construction Variations

The temperature-to-polarization leakage templates (Section 2.2.2) are constructed using linear flux weighting in our baseline analysis. We test three alternative weighting schemes: median (most robust to outliers), flat (least sensitive to source flux in the template), and quadratic (formally optimal in the case of unpolarized sources). We find that the β_{pol} measurements are stable across all weighting choices, with variations $< 0.2\sigma$ at all frequencies. This insensitivity demonstrates the effectiveness of the iterative template refinement in removing astrophysical polarization signal from the templates.

3.4.7. Source Selection Robustness

To test sensitivity to the source sample, we restrict the analysis to the 46 sources from the main field, excluding the 54 sources from summer fields. This removes sources from the shallower summer-time observations. Table 1 shows that the resulting β_{pol} constraints remain consistent with the full sample, though with slightly increased uncertainties due to the smaller sample size.

4. RESULTS

4.1. β_{pol} Measurements

Our primary measurements, along with systematic cross-checks, are summarized in Table 1 and visualized in Figure 2. We find $\beta_{\text{pol}} = 0.90 \pm 0.10$ at 95 GHz, 1.01 ± 0.12 at 150 GHz, and 0.81 ± 0.29 at 220 GHz (baseline row). These values are consistent with $\beta_{\text{pol}} = 1$ —indicating fully polarized sidelobes—at 1.0σ , 0.1σ , and 0.7σ respectively. When considering the three bands jointly, the simultaneous measurement deviates from the fully polarized case ($\beta_{\text{pol}}^{95} = \beta_{\text{pol}}^{150} = \beta_{\text{pol}}^{220} = 1$) by 1.1σ . The 220 GHz constraint is substantially weaker due to lower mapping speed and lower total polarized point source emission in this band.

Figure 3 illustrates the quality of our fits using a representative bright source at 95 GHz. The three rows display Stokes T , Q , and U parameters, while columns show observed data, best-fit β_{pol} model, and residuals. The model accurately reproduces the observed polarization pattern, with residuals consistent with noise expectations. The azimuthally symmetric beam model leaves structured residuals in Stokes T due to the beam’s true asymmetry, but this effect is not detectable in Stokes Q and U given its low intrinsic polarization fraction ($\approx 1.2\%$).

We validate the robustness of these measurements through extensive systematic tests (Section 3.4), with results shown in the subsequent rows of Table 1. For algorithmic choices that preserve the statistical power of the dataset, the results are stable to better than 0.2σ . Methodological variations that significantly alter the estimator’s precision yield central values that shift but remain statistically consistent with the baseline given their substantially larger uncertainties.

The real-space χ^2 formulation yields results consistent with the baseline, though with significantly larger uncertainties (factor of $\sim 2\text{--}4$ increase). This degradation in precision arises because the real-space covariance assumes pixel independence, failing to down-weight the noisy large-scale atmospheric and CMB fluctuations that dominate the variance. Two alternative precision matrix models in Fourier space show tighter agreement: the fully data-driven and diagonal data-driven models

Test Category	Variation	95 GHz	150 GHz	220 GHz
Baseline	—	0.904 ± 0.098	1.013 ± 0.121	0.813 ± 0.287
χ^2 Space	Real-space	0.720 ± 0.401	0.748 ± 0.355	0.932 ± 0.463
Leakage Template	Median weighting	0.926 ± 0.094	1.035 ± 0.119	0.799 ± 0.287
	Flat weighting	0.921 ± 0.103	1.021 ± 0.125	0.806 ± 0.290
	Quadratic weighting	0.898 ± 0.098	1.011 ± 0.119	0.843 ± 0.282
Precision Matrix	White noise	0.607 ± 0.353	0.700 ± 0.271	0.762 ± 0.401
	Full data-driven	0.879 ± 0.084	1.027 ± 0.129	0.873 ± 0.329
	Data-driven diagonal	0.825 ± 0.125	1.038 ± 0.120	0.691 ± 0.330
Data Selection	Main field only	0.847 ± 0.118	0.940 ± 0.105	0.669 ± 0.327
	2019–20, no τ decon	0.887 ± 0.223	1.087 ± 0.171	0.916 ± 0.393
Inference Method	Bayesian (MCLMC)	0.930 ± 0.112	1.037 ± 0.077	0.912 ± 0.240

Table 1. Measurements of β_{pol} under various analysis choices, demonstrating robustness of the baseline result to methodological variations. All systematic tests yield results consistent with the baseline within statistical uncertainties. Real-space analyses and white noise assumptions yield substantially larger uncertainties but remain consistent with the baseline. The tight agreement across leakage template constructions validates the iterative refinement procedure. The data-driven precision matrices demonstrate that the band-band-Stokes-Stokes correlations are of relatively minor importance to the overall β_{pol} constraints. The Bayesian-frequentist comparison shows that these results are not very sensitive to the statistical framework.

yield results within 0.2σ of the baseline. The “white noise” Fourier analysis, which assumes a constant precision matrix (excluding the $\vec{k} = 0$ mode), yields results and uncertainties comparable to the real-space analysis. The broad consistency between the baseline, real-space, alternative precision, and white-noise results confirms that our measurement is not driven by specific details of the noise modeling, although accurate covariance estimation is required to achieve high precision.

Leakage template construction proves remarkably stable, with all four weighting schemes (median, flat, linear, quadratic) yielding measurements within 0.2σ of each other at all bands. This insensitivity validates the iterative template refinement procedure, confirming that residual astrophysical polarization signal has been effectively removed from the templates. Similarly, restricting the analysis to the 46 sources from the main field—excluding the 54 shallower summer field sources—yields consistent results with modestly increased uncertainties, demonstrating that no particular subset of sources drives the measurement.

The agreement between frequentist (bootstrap) and Bayesian (MCLMC posterior sampling) approaches further validates our uncertainty estimation. The Bayesian credible intervals are consistent with bootstrap confidence intervals at all frequencies. This consistency confirms that the likelihood surface is well-approximated by a multivariate Gaussian, justifying our use of maximum-likelihood estimation with bootstrap resampling.

4.2. Source of β_{pol} Precision

To understand which parts of the data drive the β_{pol} constraints and to inform future analyses, we decompose

the χ^2 curvature with respect to β_{pol} (conditional likelihood) by computing partial sums across sources, Fourier modes, and Stokes parameters.

Stokes Q and U contribute asymmetric constraining power, with Q providing approximately 60% and U providing 40% of the total. This asymmetry arises from the azimuthal structure of the precision matrix. Modes approximately aligned with the k_x and k_y axes suffer contamination from low- ℓ fluctuations coupled in by the square window function. For Stokes Q , primary CMB E -mode power further degrades these modes, leaving the diagonal directions (along $k_x \pm k_y$) relatively clean and highly informative. In Stokes U , the noise contributions from mask coupling and CMB E -mode power affect complementary mode orientations, resulting in more uniform but overall lower precision when summed across the Fourier plane.

The radial ℓ -dependence reveals that intermediate angular scales provide most of the constraining power. The monopole ($\ell = 0$) contributes $<1\%$ of the total curvature; source-to-source flux variations show this mode to be too noisy to constrain the subtle effects of β_{pol} . Low- ℓ modes ($\ell < 3000$) contribute approximately 45% of the total precision on β_{pol}^{95} and β_{pol}^{220} , and $\sim 30\%$ on β_{pol}^{150} . The cumulative curvature reaches $>90\%$ of its asymptotic value by $\ell = 13,000$ across all three bands, indicating that modes above $\ell \sim 15,000$ add minimal constraining power on β_{pol} .

Individual sources contribute heterogeneously but without extreme outliers. The most constraining source (SPT-S J025329-5441.8 at 150 GHz) provides 12% of the total precision, while no other single source exceeds 7%. For comparison, uniform contribution across 100

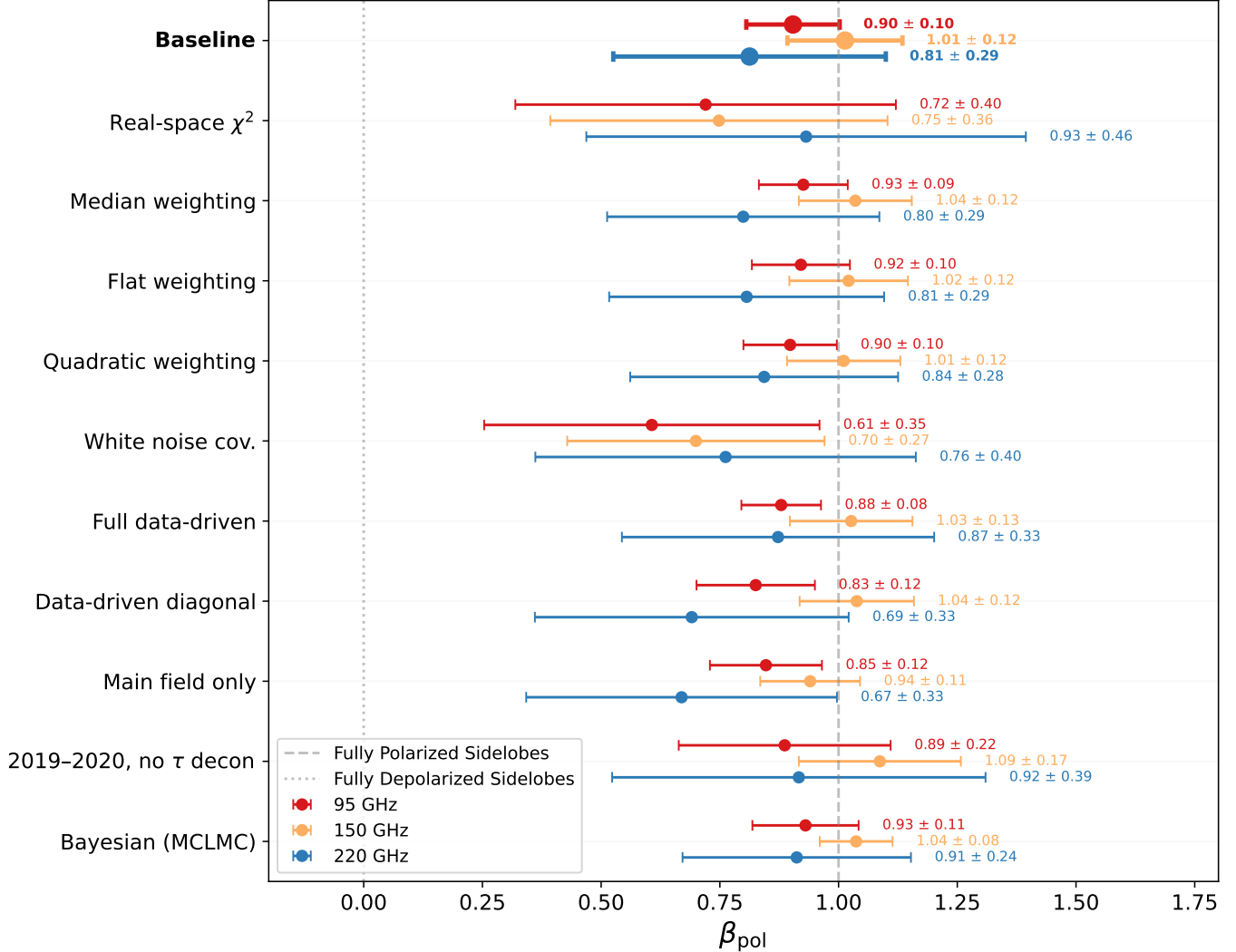


Figure 2. Visualization of Table 1. Points indicate the maximum-likelihood values (or posterior means for the Bayesian case), and error bars denote 1σ uncertainties (bootstrap or posterior standard deviation). The results are consistent across all variations, with the real-space and white-noise analyses yielding larger uncertainties as expected due to their suboptimal weighting of atmospheric noise. The tight agreement across leakage template methods and data subsets confirms that the measurement is not driven by specific analysis choices or source sub-populations.

sources would yield 1% per source. This moderate heteroskedasticity validates our methodological choices of the source-averaged construction of leakage templates and the use of bootstrap resampling for uncertainty estimation.

4.3. B-spline Beam Profiles

To assess the goodness of fit of the β_{pol} model to the polarized beam measurements, we fit the highly parametric regularized B-spline model defined in Section 3.1.1 and examine the resulting radial beam profiles.

Figure 4 displays these profiles. Unlike the β_{pol} parameterization, the B-spline model imposes no constraints on the relationship between the temperature

and polarization beam shapes beyond the central $0.25'$. The temperature beams (top panels) are characterized with high precision across the full radial range. The polarization beams (bottom panels) exhibit fractional uncertainties approximately 50 times larger, a direct consequence of the low intrinsic polarization fractions ($\sim 2\%$) of the extragalactic source population.

Despite these larger uncertainties, the reconstructed polarization profiles track the temperature profiles at all three frequencies, remaining consistent with the $\beta_{\text{pol}} \approx 1$ case (dotted lines). While the B-spline model possesses the freedom to fit complex radial features, no unexpected structure is observed. We conclude that the po-

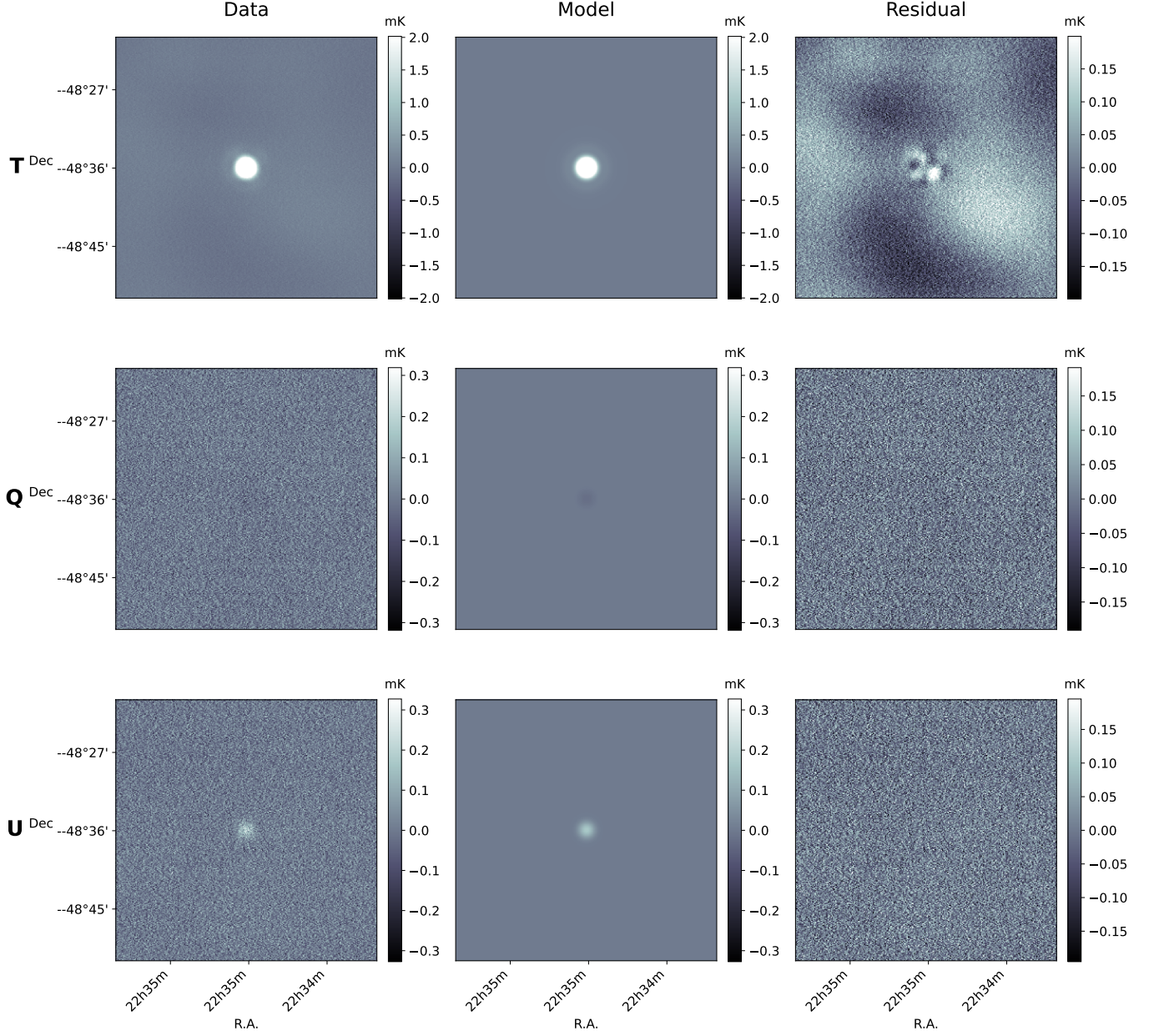


Figure 3. Example of a typical bright polarized point source in SPT-3G observations at 95 GHz. Rows show Stokes T , Q , and U parameters. Columns display the observed data, best-fit β_{pol} model, and residuals. The color scales are in units of mK_{CMB} , where one unit corresponds to the flux density needed to make the CMB appear 1 mK brighter at 95 GHz. The azimuthally symmetric model leaves residuals in Stokes T due to the asymmetric nature of the beam. Stokes Q and U do not show any residuals at the source location.

larization beam measurements are consistent with the temperature beam.

Figure 5 presents the same reconstruction in the harmonic domain. As detailed in the curvature analysis of Section 4.2, low-multipole data ($\ell < 3000$) provide a subdominant fraction of the total constraining power—approximately 45%, 30%, and 45% of the total precision at 95, 150, and 220 GHz, respectively. This distribution of statistical weight is visually apparent in the figure:

while the absolute difference between the fully polarized and depolarized models is largest at $\ell < 3000$, the measurement uncertainties (indicated by the spread of bootstrap realizations) are substantial in that regime. For instance, the $\ell = 0$ intercept of the 95 GHz temperature beam shows a small but statistically significant systematic offset between the measured B-spline profile and the $\beta_{\text{pol}} = 1$ prediction (derived from the Saturn-combined B_{full}). However, since this mode (cor-

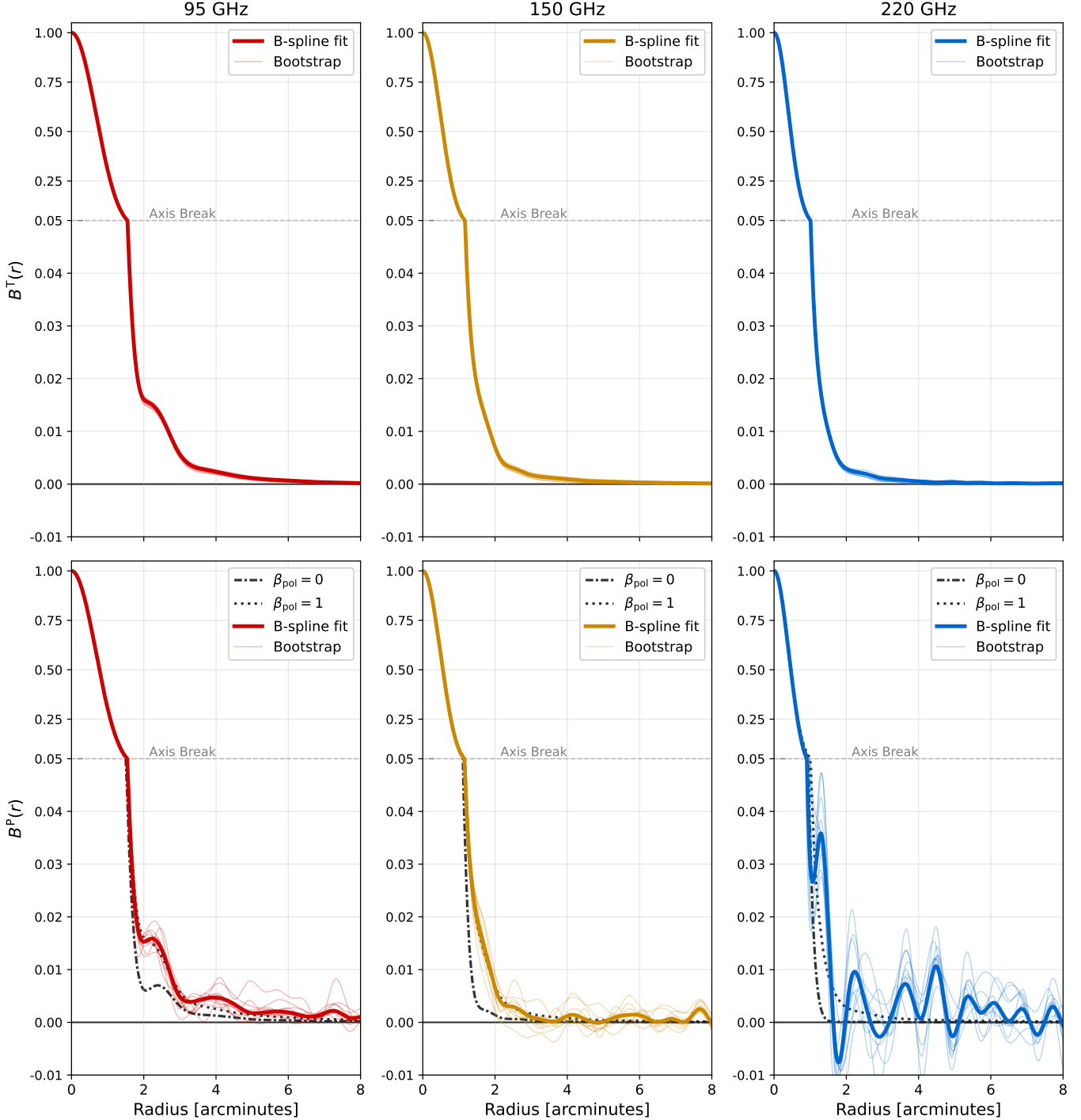


Figure 4. Temperature (top) and polarization (bottom) radial beam profiles reconstructed using the B-spline basis. These profiles are peak-normalized such that $B(r = 0) = 1$. Thick colored curves show the best-fit profiles for 95 GHz (red), 150 GHz (gold), and 220 GHz (blue). Thin colored lines show a subset of the 200 bootstrap realizations, illustrating the measurement uncertainty. The polarization beam uncertainties are approximately 50 times larger than temperature beam uncertainties due to the $\sim 2\%$ intrinsic polarization fraction of most sources. Overlaid on the polarization beams are predictions from the β_{pol} model for two limiting cases: fully depolarized sidelobes ($\beta_{\text{pol}} = 0$, dot-dashed black) and fully polarized sidelobes ($\beta_{\text{pol}} = 1$, dotted black). The model-independent B-spline fits closely track the $\beta_{\text{pol}} = 1$ prediction, showing no evidence of significant depolarization.

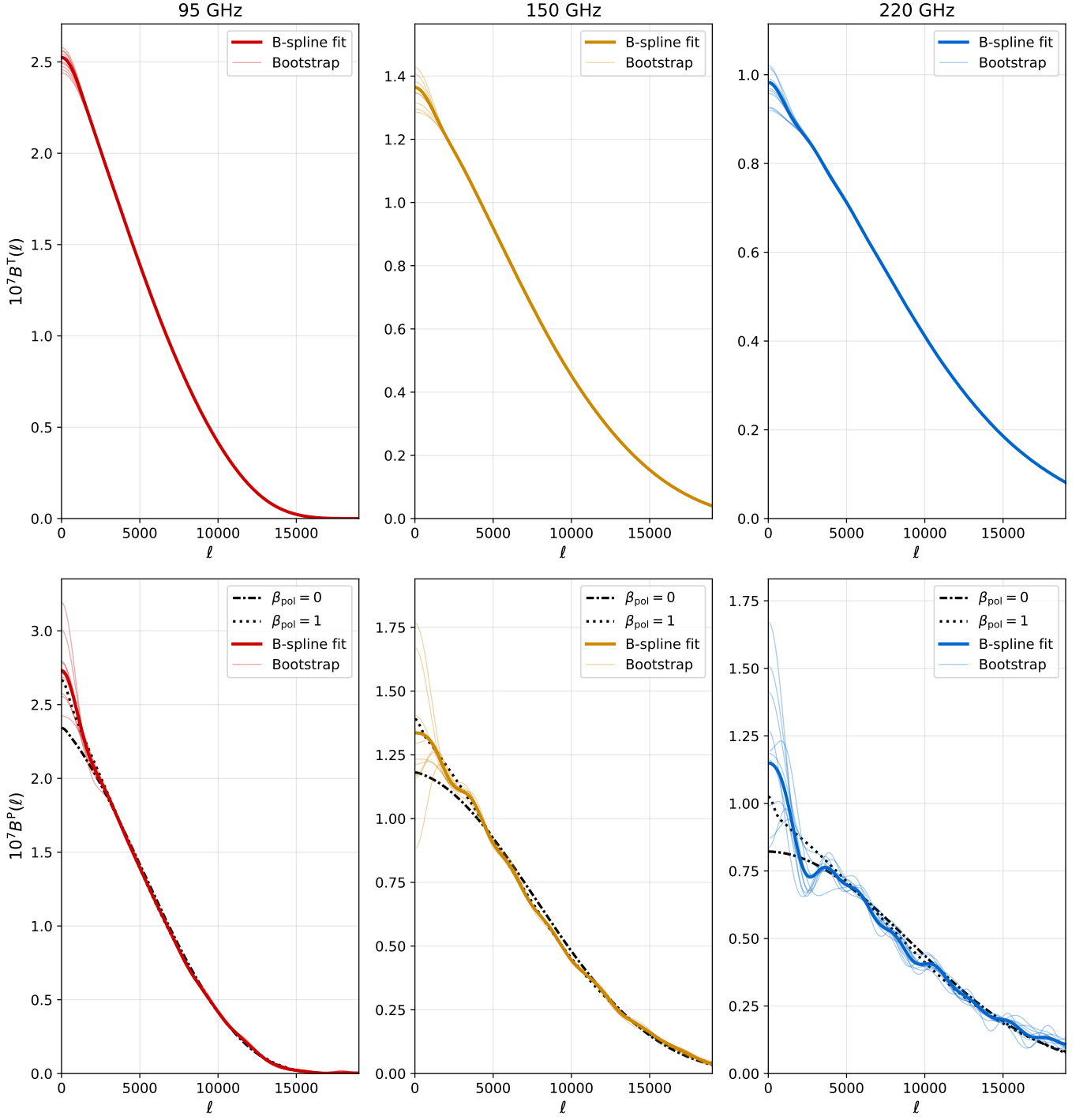


Figure 5. Harmonic domain representation of the beam profiles shown in Figure 4. The curves are obtained via Hankel transformation of the real-space B-spline fits and contain equivalent information. The profiles retain the real-space peak normalization $B(r = 0) = 1$, corresponding to $\int \ell B(\ell) d\ell = 2\pi$.

responding to the average of the $0.5^\circ \times 0.5^\circ$ map) has a large uncertainty, such a systematic error has negligible impact on the β_{pol} constraints. Instead, the majority of the constraining power comes from the range $3000 \lesssim \ell \lesssim 10,000$, where the tighter observational constraints allow for a precise measurement of the shape of $B(\ell)$. This indicates that the source of our point source-based constraints on β_{pol} differs somewhat from that of C25, which determined β_{pol} using the CMB power spectrum in the $400 < \ell < 4000$ range. While the β_{pol} parameterization prescribes a specific scale dependence based on the temperature beam morphology and the physical optics modeling, the true polarized beam could follow a different profile. An alternative model could potentially reconcile these measurements by allowing the polarization response to deviate from the model prediction at low multipoles, while maintaining the consistency with the temperature beam observed at the high multipoles probed here. Under such a scenario, the apparent discrepancy would reflect the limitations of the single-parameter β_{pol} model when applied to datasets sensitive to distinct angular regimes.

4.4. Comparison with Previous Constraints

We compare our direct, point source-based measurements of the optical beam with the constraints previously derived from CMB power spectrum analyses in C25. To perform a rigorous statistical comparison, we extract the publicly available SPT-3G 2019–2020 (“D1”) Λ CDM chain from [LAMBDA](#) and construct the three-dimensional posterior distribution $P(\beta_{\text{pol}}^{95}, \beta_{\text{pol}}^{150}, \beta_{\text{pol}}^{220})$. We fit a trivariate Gaussian to a gridded histogram of the posterior samples, effectively extrapolating beyond the $\beta_{\text{pol}} \in [0, 1]$ prior used in C25 to allow comparison with our point source constraints that extend outside this range.

Considering the diagonals of the trivariate Gaussian, we find $\beta_{\text{pol}} = 0.37 \pm 0.19$ at 95 GHz, 0.49 ± 0.27 at 150 GHz, and 0.55 ± 0.21 at 220 GHz as the 68% credible intervals from the C25 CMB power spectrum analysis. Comparing these to our baseline results (Table 1), we find that the point source data consistently prefer higher β_{pol} values, indicating less depolarization than inferred from the power spectrum. To quantify the agreement in three dimensions, we calculate the Mahalanobis distance $\sqrt{(\vec{\mu}_{\text{PS}} - \vec{\mu}_{\text{C25}})^T (\mathbf{C}_{\text{PS}} + \mathbf{C}_{\text{C25}})^{-1} (\vec{\mu}_{\text{PS}} - \vec{\mu}_{\text{C25}})}$, where $\vec{\mu}_{\text{PS}}$ and \mathbf{C}_{PS} refer to the parameter vector and covariance from the point source analysis in this work, and $\vec{\mu}_{\text{C25}}$ and \mathbf{C}_{C25} refer to those from C25. We find an equivalent significance of 1.9σ ($p = 0.06$), which does not meet standard thresholds for claiming statistical in-

consistency (e.g., 3σ or $p < 0.01$); we therefore describe the results as being in mild tension.

When measured against only the point source covariance, the C25 best-fit parameters lie at a distance of 5.9σ , while the point source best-fit values lie at a distance of 4.0σ from the C25 posterior. Each analysis thus rules out the other’s central value, yet the combined constraint allows a compromise solution at $p = 0.06$. If not a statistical fluctuation, one possible interpretation is that the β_{pol} parameter in the power spectrum analysis may have absorbed non-beam systematics. Alternatively, the mild tension may reflect a limitation of the β_{pol} sidelobe model. A physically motivated beam model that exhibits depolarization at low multipoles, where the power spectrum analysis has greatest sensitivity, while remaining consistent with the temperature beam at the high multipoles probed by point sources, could potentially reconcile the two measurements.

Figure 6 shows the one- and two-dimensional projections of these three-dimensional constraints. While there is overlap in the 95% confidence regions, the C25 contours (blue) are systematically offset toward lower values compared to the point source contours (orange). The two methods probe β_{pol} through entirely different physical effects: our analysis measures the radial beam profile directly from bright sources, while the cosmological analysis infers β_{pol} through its effect on large-scale CMB power spectra. The direct measurement suggests that the actual optical depolarization is minimal.

To assess whether methodological differences in time constant treatment or data selection contribute to this offset, we performed a retrospective check using only 2019–2020 data processed without time constant deconvolution, matching the methodology of C25. Crucially, this analysis uses the exact same beam profiles $B_{\text{main}}(r)$ and $B_{\text{full}}(r)$ used in C25, meaning β_{pol} implies precisely the same radial profile as in that work (in contrast to our primary analysis, which interpolates between optical beam profiles constructed after time constant deconvolution). We find $\beta_{\text{pol}}^{95} = 0.89 \pm 0.22$, $\beta_{\text{pol}}^{150} = 1.09 \pm 0.17$, and $\beta_{\text{pol}}^{220} = 0.92 \pm 0.39$. The Mahalanobis distance to the C25 constraint becomes 1.1σ , down from 1.9σ in our primary analysis. This reduction is driven by the larger statistical uncertainties expected from the reduced data volume, rather than any significant shift in the central values. This lack of significant shift supports our expectations that the instrument beam is stable over the 2019–2023 observing period, and that the β_{pol} parameter provides a self-consistent measure of physical sidelobe depolarization, whether time constant effects are included in the beam model or deconvolved from the TOD.

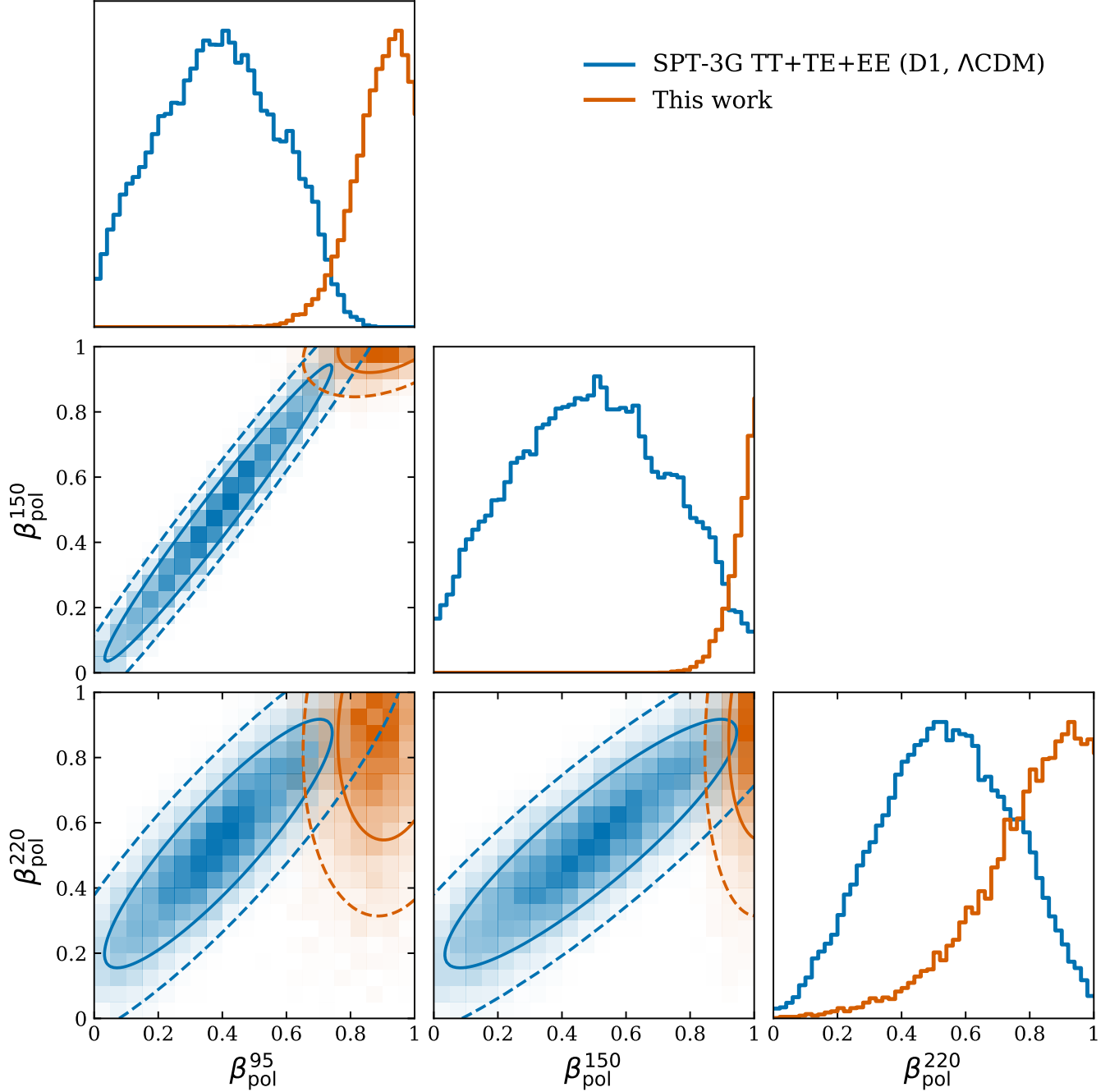


Figure 6. Comparison of β_{pol} measurements from this work (orange; Bayesian results from Table 1) with values inferred from the C25 cosmological power spectrum analysis (blue). The 1D histograms and color density grids display the distribution of MCMC samples, while the 2D contours correspond to the 68% and 95% regions of a multivariate Gaussian fit to those samples. Although the distributions overlap, they are in mild tension (1.9σ). The direct point source measurements are consistent with no sidelobe depolarization ($\beta_{\text{pol}}^{95} = \beta_{\text{pol}}^{150} = \beta_{\text{pol}}^{220} = 1$), a conclusion that was disfavored at 5σ in the C25 power spectrum analysis.

5. DISCUSSION

5.1. Physical Interpretation

Our direct measurements from polarized point sources yield $\beta_{\text{pol}} = 0.90 \pm 0.10$ at 95 GHz, 1.01 ± 0.12 at 150 GHz, and 0.81 ± 0.29 at 220 GHz, consistent with unity across all frequencies. These results indicate that SPT-3G beam sidelobes preserve polarization nearly as efficiently as the main beam, with the data constraining any depolarization to $\lesssim 20\%$ at 95 and 150 GHz.

The consistency with $\beta_{\text{pol}} \approx 1$ constrains the physical mechanisms that produce beam sidelobes. Processes that destroy polarization information, such as diffuse scattering from rough surfaces or baffling materials, are incompatible with our measurements. Instead, the data favor coherent optical processes that preserve the polarization state of incident radiation. Diffraction at aperture edges and specular reflections from telescope structures are both coherent processes that do not stochastically scramble the polarization signal. Our measurements indicate that such polarization-preserving processes in the SPT-3G optical system are responsible for producing the observed sidelobe.

5.2. Implications for Cosmological Analysis

The mild tension between our point source measurements and the cosmological constraints of C25 warrants careful interpretation. While the statistical disagreement is only 1.9σ , it is striking that the direct measurements from point sources point to polarization beams that are entirely consistent with the temperature beams, while C25 rejected this null hypothesis at 5σ . This observed discrepancy admits three explanations. First, it may simply be a statistical fluctuation. Second, it may point to a limitation of the beam model itself; the power spectrum constraints are driven by low multipoles ($\ell \lesssim 3000$) while our analysis derives the majority of its constraining power from higher multipoles ($3000 \lesssim \ell \lesssim 10,000$), suggesting that a more complex polarized beam profile could reconcile the two measurements. Third, the difference may stem from residual systematics in the power spectrum analysis unrelated to the optical beam being absorbed into the β_{pol} parameter.

Despite this ambiguity, these measurements provide valuable inputs for future SPT-3G cosmological analyses. Previous analyses demonstrated that marginalizing over β_{pol} with uninformative priors degrades constraints on cosmological parameters including the Hubble constant, baryon density, and scalar spectral index. Our measurements substantially reduce the allowed parameter volume, providing future SPT-3G power spectrum analyses with a $\delta\beta_{\text{pol}} \sim 0.1$ prior at 95 and 150 GHz,

compared to the $[0, 1]$ range previously used. These informative priors have the potential to sharpen cosmological constraints by breaking the beam-cosmology degeneracies identified in previous works. However, realizing this potential requires determining which of the three explanations above is correct. Resolving whether the observed tension arises from statistical fluctuations, beam modeling limitations, unrelated systematics, or any combination thereof will dictate how these priors are applied in future analyses, and motivates a rigorous search for alternative optical or non-optical systematic explanations for the inter-frequency features observed in the CMB power spectrum.

6. CONCLUSIONS

We have measured the polarization beam response of SPT-3G using 100 bright polarized point sources observed from 2019 through 2023. The sidelobe polarization efficiency parameter β_{pol} is constrained to 0.90 ± 0.10 at 95 GHz, 1.01 ± 0.12 at 150 GHz, and 0.81 ± 0.29 at 220 GHz. These measurements are consistent with fully polarized sidelobes ($\beta_{\text{pol}} = 1$).

Extensive systematic tests validate these results. The measurements prove stable across alternative statistical formulations (real-space versus Fourier-space), different covariance treatments, variations in leakage template construction, and alternative source selections. The agreement between frequentist bootstrap and Bayesian posterior sampling confirms that uncertainties are well characterized. The B-spline analysis provides complementary highly parametric beam profiles that qualitatively agree between temperature and polarization, further supporting the $\beta_{\text{pol}} \approx 1$ case.

Comparing these results with the β_{pol} values inferred from previous cosmological power spectrum analyses (C25), we find a mild (1.9σ) tension. While the power spectrum analysis favored $\beta_{\text{pol}} \sim 0.5$, our direct measurements favor $\beta_{\text{pol}} \approx 1$, indicating that the physical beam sidelobes are not significantly depolarized. This difference could stem from residual systematics in the power spectrum analysis unrelated to the optical beam being absorbed into the β_{pol} parameter. Alternatively, the difference may reflect the distinct angular scales probed by each analysis. The β_{pol} constraints from the power spectrum are primarily driven by low multipoles ($\ell < 3000$), whereas our point source analysis derives the majority of its constraining power from the range $3000 \lesssim \ell \lesssim 10,000$, allowing for a more precise measurement of the shape of $B(\ell)$ at high multipoles. Therefore, the difference in β_{pol} constraints may point to a limitation of the beam model itself; a more complex polarized beam profile that deviates from the temperature beam

only at large angular scales could potentially reconcile the two measurements.

These constraints provide valuable inputs for future SPT-3G cosmological analyses. However, realizing their potential to break beam-cosmology degeneracies requires determining which of the three explanations above is correct. By establishing polarization beam properties independently of cosmological modeling, we aim to prevent beam nuisance parameters from absorbing residual systematics or biasing cosmological inferences, and enable sharper constraints on parameters including the Hubble constant, scalar spectral index, and baryon density that would otherwise suffer degeneracies with beam uncertainties. Our methodology demonstrates that bright polarized point sources can constrain polarized beam systematics with $\sim 10\%$ precision, comparable to the precision achieved through the cosmological analyses themselves.

The computational framework developed here, including GPU-accelerated fitting and modern optimization techniques, provides a template applicable to other high-resolution CMB experiments requiring precise beam characterization. Future SPT configurations, including the planned SPT-3G+ upgrade, will require new polarized beam measurements, and the analysis framework established in this work can be directly applied to characterize these upgraded instruments, ensuring continuity in beam systematics control as the SPT project advances.

ACKNOWLEDGMENTS

The South Pole Telescope program is supported by the National Science Foundation (NSF) through awards

OPP-1852617 and OPP-2332483. Partial support is also provided by the Kavli Institute of Cosmological Physics at the University of Chicago. This research was done using services provided by the OSG Consortium (R. Pordes et al. 2007; I. Sfiligoi et al. 2009; OSG 2006, 2015), which is supported by the National Science Foundation awards #2030508 and #2323298. The GPU resources used in this work were provided by the QUP World Premiere Institute. Argonne National Laboratory’s work was supported by the U.S. Department of Energy, Office of High Energy Physics, under contract DE-AC02-06CH11357. The UC Davis group acknowledges support from Michael and Ester Vaida. Work at the Fermi National Accelerator Laboratory (Fermilab), a U.S. Department of Energy, Office of Science, Office of High Energy Physics HEP User Facility, is managed by Fermi Forward Discovery Group, LLC, acting under Contract No. 89243024CSC000002. The Melbourne authors acknowledge support from the Australian Research Council’s Discovery Project scheme (No. DP210102386). The Paris group has received funding from the European Research Council (ERC) under the European Union’s Horizon 2020 research and innovation program (grant agreement No 101001897), and funding from the Centre National d’Etudes Spatiales. The SLAC group is supported in part by the Department of Energy at SLAC National Accelerator Laboratory, under contract DE-AC02-76SF00515.

REFERENCES

Ade, P. A. R., Ahmed, Z., Amiri, M., et al. 2021, *PhRvL*, 127, 151301, doi: [10.1103/PhysRevLett.127.151301](https://doi.org/10.1103/PhysRevLett.127.151301)

Archipley, M., Hryciuk, A., Bleem, L. E., et al. 2025, arXiv e-prints, arXiv:2506.00298, doi: [10.48550/arXiv.2506.00298](https://doi.org/10.48550/arXiv.2506.00298)

Benson, B. A., Ade, P. A. R., Ahmed, Z., et al. 2014, in *Proc. SPIE*, Vol. 9153, Millimeter, Submillimeter, and Far-Infrared Detectors and Instrumentation for Astronomy VII, 91531P, doi: [10.1117/12.2057305](https://doi.org/10.1117/12.2057305)

Camphuis, E., Quan, W., Balkenhol, L., et al. 2025, arXiv e-prints, arXiv:2506.20707, doi: [10.48550/arXiv.2506.20707](https://doi.org/10.48550/arXiv.2506.20707)

CMB-S4/SPT-3G Collaboration. 2024, *spt3g_software: Analysis software for the South Pole Telescope*, 0.4 GitHub. https://github.com/CMB-S4/spt3g_software

Ge, F., Millea, M., Camphuis, E., et al. 2025, *Phys. Rev. D*, 111, 083534, doi: [10.1103/PhysRevD.111.083534](https://doi.org/10.1103/PhysRevD.111.083534)

Hoffman, M. D., & Gelman, A. 2011, *The No-U-Turn Sampler: Adaptively Setting Path Lengths in Hamiltonian Monte Carlo*, arXiv, doi: [10.48550/arXiv.1111.4246](https://doi.org/10.48550/arXiv.1111.4246)

Kingma, D. P., & Ba, J. 2017, *Adam: A Method for Stochastic Optimization*, arXiv, doi: [10.48550/arXiv.1412.6980](https://doi.org/10.48550/arXiv.1412.6980)

Lewis, A., Challinor, A., & Lasenby, A. 2000, *Astrophys. J.*, 538, 473

OSG. 2006, OSGPool, OSG, doi: [10.21231/906P-4D78](https://doi.org/10.21231/906P-4D78)

OSG. 2015, Open Science Data Federation, OSG, doi: [10.21231/0KVZ-VE57](https://doi.org/10.21231/0KVZ-VE57)

Planck Collaboration, Aghanim, N., Akrami, Y., et al. 2020a, *A&A*, 641, A8, doi: [10.1051/0004-6361/201833886](https://doi.org/10.1051/0004-6361/201833886)

Planck Collaboration, Aghanim, N., Akrami, Y., et al. 2020b, *A&A*, 641, A6, doi: [10.1051/0004-6361/201833910](https://doi.org/10.1051/0004-6361/201833910)

Pordes, R., et al. 2007, *J. Phys. Conf. Ser.*, 78, 012057, doi: [10.1088/1742-6596/78/1/012057](https://doi.org/10.1088/1742-6596/78/1/012057)

Prabhu, K., Raghunathan, S., Millea, M., et al. 2024, *ApJ*, 973, 4, doi: [10.3847/1538-4357/ad5ff1](https://doi.org/10.3847/1538-4357/ad5ff1)

Qu, F. J., Sherwin, B. D., Madhavacheril, M. S., et al. 2024, *ApJ*, 962, 112, doi: [10.3847/1538-4357/acfe06](https://doi.org/10.3847/1538-4357/acfe06)

Reddi, S. J., Kale, S., & Kumar, S. 2019, On the Convergence of Adam and Beyond, arXiv, doi: [10.48550/arXiv.1904.09237](https://doi.org/10.48550/arXiv.1904.09237)

Robnik, J., Luca, G. B. D., Silverstein, E., & Seljak, U. 2023, Microcanonical Hamiltonian Monte Carlo, arXiv, doi: [10.48550/arXiv.2212.08549](https://doi.org/10.48550/arXiv.2212.08549)

Sfiligoi, I., Bradley, D. C., Holzman, B., et al. 2009, in 2, Vol. 2, 2009 WRI World Congress on Computer Science and Information Engineering, 428–432, doi: [10.1109/CSIE.2009.950](https://doi.org/10.1109/CSIE.2009.950)

Sobrin, J. A., Anderson, A. J., Bender, A. N., et al. 2022, *ApJS*, 258, 42, doi: [10.3847/1538-4365/ac374f](https://doi.org/10.3847/1538-4365/ac374f)

Tristram, M., Banday, A. J., Górski, K. M., et al. 2022, *PhRvD*, 105, 083524, doi: [10.1103/PhysRevD.105.083524](https://doi.org/10.1103/PhysRevD.105.083524)

Zebrowski, J. A., Reichardt, C. L., Anderson, A. J., et al. 2025, arXiv e-prints, arXiv:2505.02827, doi: [10.48550/arXiv.2505.02827](https://doi.org/10.48550/arXiv.2505.02827)